Self-Induced Ultrafast Electron-Hole-Plasma Temperature Oscillations in Nanowire Lasers

Andreas Thurn[1,*] Jochen Bissinger,[1] Stefan Meinecke,[2] Paul Schmiedeke,[1] Sang Soon Oh,[3] Weng W. Chow,[4] Kathy Lüdge,[5] Gregor Koblmüller,[1] and Jonathan J. Finley[1,†]

[1] *Walter Schottky Institut, Technische Universität München, Am Coulombwall 4, Garching 85748, Germany*

[2] *Institut für Theoretische Physik, Technische Universität Berlin, Hardenbergstraße 36, Berlin 10623, Germany*

[3] *School of Physics and Astronomy, Cardiff University, Cardiff CF24 3AA, United Kingdom*

[4] *Sandia National Laboratories, Albuquerque, New Mexico 87185-1086, USA*

[5] *Institut für Physik, Technische Universität Ilmenau, Weimarer Straße 25, Ilmenau 98693, Germany*

Nanowire lasers can be monolithically and site-selectively integrated onto silicon photonic circuits. To assess their full potential for ultrafast optoelectronic devices, a detailed understanding of their lasing dynamics is crucial. However, the roles played by their resonator geometry and the microscopic processes that mediate energy exchange between the photonic, electronic, and phononic subsystems are largely unexplored. Here, we study the dynamics of GaAs-AlGaAs core-shell nanowire lasers at cryogenic temperatures using a combined experimental and theoretical approach. Our results indicate that these NW lasers exhibit sustained intensity oscillations with frequencies ranging from 160 GHz to 260 GHz. As the underlying physical mechanism, we have identified self-induced electron-hole plasma temperature oscillations resulting from a dynamic competition between photoinduced carrier heating and cooling via phonon scattering. These dynamics are intimately linked to the strong interaction between the lasing mode and the gain material, which arises from the wavelength-scale dimensions of these lasers. We anticipate that our results could lead to optimised approaches for ultrafast intensity and phase modulation of chip-integrated semiconductor lasers at the nanoscale.

I. INTRODUCTION

Nanowires (NWs) provide a unique approach to site-selectively and epitaxially integrate direct-gap semiconductors onto silicon [1–4]. Optically pumped lasing has been demonstrated at room temperature using III-V and II-VI compound semiconductors [5–7], and group-III nitrides [8], with emission wavelengths that can be tuned from the ultraviolet to the near-infrared spectral range [5–16]. Thus, they are promising candidates for on-chip lasers in photonic integrated circuits. To further their development, a detailed understanding of their lasing dynamics is essential. Previous studies have laid the groundwork by investigating several aspects of carrier relaxation, gain dynamics, plasmonic and coherent phenomena, and the role of lattice defects in a number of different material systems [17–23]. Despite these advances, however, the microscopic mechanisms and dynamic processes that ultimately determine, and possibly limit, their potential for ultrafast optoelectronic devices have remained largely unexplored.

Here, we investigate the microscopic lasing dynamics of GaAs-AlGaAs core-shell NW lasers [3,5,23] and present evidence for ultrafast intensity and phase oscillations, caused by an exceptionally strong nonequilibrium analogue of relaxation oscillations [24], with frequencies ranging from 160 GHz to 260 GHz. Previous work has proposed Rabi oscillations to explain the observed dynamics [23]. However, this interpretation is challenged by the dephasing time in an electron-hole plasma, which is on the order of 100 fs [25–29], significantly shorter than the value used in Ref. [23]. We show that these unique nonequilibrium dynamics are enabled by the miniaturized dimensions of these lasers and the resulting competition between carrier heating and cooling during lasing operation. Our results are supported by complementary microscopic simulations based on a quantum statistical [30] and a semiconductor Bloch model [31] (see Sec. IV).

*andreas.thurn@wsi.tum.de

†finley@wsi.tum.de

II. RESULTS

A. Pump-probe measurement and simulation

Femtosecond pump-probe spectroscopy was performed on single NWs with a carefully timed pair of pump and probe pulses, separated by a time delay Δt. Details on the optical characterization and growth of the NWs are summarized in Sec. IV.

Figure 1(a) illustrates our pump-probe excitation scheme. The pump pulse power (P_{pump}) and probe pulse power (P_{probe}) are above and below the threshold (P_{th}) of the NW laser, respectively. After excitation, the NW laser emits two modulated output pulses, separated by a time delay $\Delta\tau$. Figure 1(b) shows an optical-microscope image of the NW laser studied in this work (length $L \sim 10\ \mu$m) during lasing operation. Its emission is dominated by a single mode at an energy of approximately 1.51 eV (see Sec. I of the Supplemental Material [32]) and is clearly visible from both end facets. All measurements and simulations have been performed at a lattice temperature of $T_L = 10$ K, with an initial electron excess energy of approximately 60 meV and a hole excess energy of approximately 11 meV, unless specified otherwise.

Figure 1(c) presents typical results of a pump-probe measurement as a function of Δt. Here, we have normalized the spectra to their maximum value and set the excitation power to $P_{pump}/P_{th} \sim 2.7$ and $P_{probe}/P_{th} \sim 0.7$, such that the probe pulse alone cannot induce lasing. We observe a delayed onset of two-pulse interference fringes, reflecting the turn-on time (t_{on}) of the laser, which depends on both the excitation conditions *and* the initial relaxation of the photoexcited carriers [17,18,23,33]. Experimentally, $t_{on} = (6.3 \pm 0.8)$ ps was determined from the Δt dependence of the spectrally integrated mode intensity (see Sec. II of the Supplemental Material [32]), using the transient depletion of the probe absorption [17]. For increasing Δt, the interference fringes increase linearly in frequency. Their existence further shows that the weak probe pulse restarts lasing, due to which the probe-induced output pulse partially adopts the phase of the residual electric field in the cavity defined by the previous output pulse [23]. Hence, the strong pump pulse leaves considerable excitation for an extended period of time, which decays with increasing Δt. This, in turn, leads to a change in refractive index and, thus, to a pronounced red shift of the interference pattern. Meanwhile,
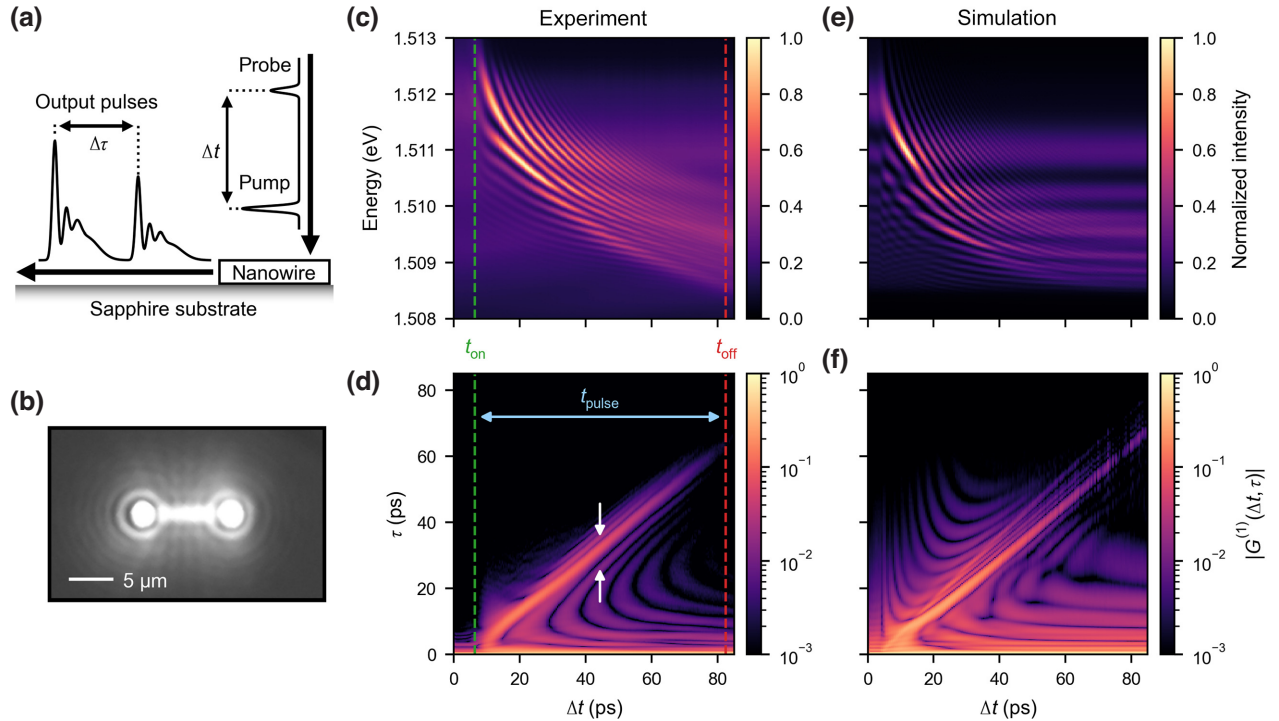

FIG. 1. The pump-probe measurement and simulation. (a) A schematic of a NW laser subject to pump-probe excitation with delay Δt, emitting two temporally asymmetric and modulated pulses, separated by $\Delta\tau$. (b) An optical-microscope image of the NW laser studied in this work, with the excitation laser filtered out. (c) Time-integrated spectra, showing typical two-pulse interference fringes with additional beating patterns along the energy axis. (d) The normalized magnitude of the electric field autocorrelation ($|G^{(1)}(\Delta t, \tau)|$), exhibiting pronounced oscillations along τ above and below the main sideband (indicated by white arrows), resulting from the beating patterns in (c). In (c) and (d), we indicate the laser turn-on time (t_{on}) and the disappearance of the sideband (t_{off}). Their difference, $t_{pulse} \sim t_{off} - t_{on}$, gives a measure of the total output-pulse length. (e),(f) The corresponding semiconductor Bloch simulation of the respective experimental data in (c) and (d).

the fringes become weaker and finally disappear at a delay $\Delta t = t_{\text{off}}$.

For ease of interpretation, we move to the time domain by Fourier transforming the energy axis in Fig. 1(c). This yields the electric field autocorrelation $G^{(1)}(\Delta t, \tau)$ as a function of Δt and the time shift τ [17,34]. Its normalized magnitude $|G^{(1)}(\Delta t, \tau)|$ is presented in Fig. 1(d) on a logarithmic scale. For normalization, we have used the respective maximum value at $\tau = 0$ for each Δt to facilitate comparison with theory. The fringes in Fig. 1(c) lead to a linear sideband, with a full width at half maximum (FWHM) of approximately 3 ps, that sets on at a delay $\Delta t = t_{\text{on}}$ and disappears at $\Delta t = t_{\text{off}}$. We have quantified $t_{\text{off}} = (82.4 \pm 0.4)$ ps as the delay time where the main sideband amplitude decreases to 1% of its maximum value. Since the photon lifetime of the resonator is < 1 ps [5], the disappearance of the main sideband marks the termination of the first NW-laser output pulse. Thus, $t_{\text{pulse}} \sim t_{\text{off}} - t_{\text{on}} = (76.1 \pm 0.9)$ ps is a measure for the overall output-pulse duration. However, in addition to the main sideband, we also observe pronounced oscillations above and below, as indicated by white arrows in Fig. 1(d). These reflect the beating patterns in the spectral interference fringes in Fig. 1(c). Weak indications of these oscillations can be found in previous work [17,23] but their significance has not been scrutinized until now. Together, the long t_{pulse}, the short FWHM of the main sideband, and the oscillations indicate that the NW output pulses are strongly asymmetric and modulated in time.

To understand the origin of the oscillating features in Fig. 1(d), we have first used the semiconductor Bloch model to simulate the experimental data. For these and all following simulations, we have used an end-facet reflectivity of $R = 0.5$ and a spontaneous-emission coupling factor of $\beta = 0.1$. Both values have been obtained using a quantum statistical simulation of the measured continuous-wave lasing characteristics of the NW under investigation (see Sec. III of the Supplemental Material [32]) and are in full accord with the literature [3,5,6,35]. The result of this semiconductor Bloch approach is presented in Figs. 1(e) and 1(f), in which we have used the same excitation powers as in the experiment. The simulation exhibits excellent qualitative agreement with all observed features of the experimental data in Figs. 1(c) and 1(d). It reproduces the delayed onset of interference fringes, the temporal asymmetry of the output pulses, and the oscillations both above and below the main sideband. Moreover, the model reveals that these originate from carrier-temperature oscillations (see Sec. IV of the Supplemental Material [32]). To obtain quantitative agreement for all features using the semiconductor Bloch model, it may be necessary to transition from the relaxation-rate approximation for the carrier dynamics to a Boltzmann-equation approach. However, due to computational limitations, such a generalized model is unfeasible in our case (see Sec. IV).

B. Quantum statistical simulation

To uncover the full significance of these oscillations and to enable a theoretical description of measurement series within which the scattering rates vary, it is necessary to go beyond the relaxation-rate approximation used in the semiconductor Bloch model. For this purpose, we have used a quantum statistical model that self-consistently calculates the rates for carrier-carrier and carrier-phonon scattering.

Figure 2 displays the results of this approach for a pump-probe excitation with $\Delta t = 40$ ps. The excitation powers used were the same as in Fig. 1. In Fig. 2(a), we present the laser intensity as a function of time and determine $t_{\text{on}} \sim 5.7$ ps as the time it takes to reach $1/e$ of the first output-pulse maximum. After turn-on, the NW pulses are observed to be strongly asymmetric in time, with a pronounced initial peak (FWHM ~ 1.3 ps), following oscillations with a frequency of $\nu_S = 222$ GHz and a long tail. This is in qualitative agreement with both the experiment and the simulation in Fig. 1. Following up on the results of the semiconductor Bloch model, we have investigated the temporal evolution of the carrier distributions by determining the instantaneous electron (T_e) and hole (T_h) temperatures for each time step (see Sec. V of the Supplemental Material [32]). Figure 2(b) shows that the carrier temperatures cool to $T_e \sim 79$ K and $T_h \sim 76$ K after $t \sim 5.3$ ps, shortly before the laser turns on, which is in full accord with the literature [36,37]. This cooling primarily takes place via scattering of carriers with longitudinal optical (LO) phonons [29,38,39]. After the first temperature minimum at $t \sim 5.3$ ps and during turn-on, we observe a pronounced initial increase of the carrier temperatures by $\Delta T_e \sim 19.8$ K and $\Delta T_h \sim 4.2$ K for electrons and holes, respectively. Subsequently, the carrier temperatures show clear oscillations with a frequency of 222 GHz, mirrored by the laser intensity in Fig. 2(a). Since T_e changes the most, we highlight in Figs. 2(a)–2(d) its first heating and cooling cycle in red and blue, respectively. As observed in Fig. 2(c), the carrier-temperature dynamics are also mirrored in the time dependence of the electron scattering rates near the lasing energy. While these time variations in the scattering rates are not necessary for the existence of the oscillations in Figs. 2(a) and 2(b), they likely do increase their strength (see Sec. IV of the Supplemental Material [32]). Near t_{on}, the carrier-carrier scattering rate of electrons is $\gamma_{\text{cc},e} \sim 8.6$ ps^{-1}, while the electron-LO-phonon scattering rate is $\gamma_{e\text{-ph}} \sim 0.3$ ps^{-1}. In contrast to the oscillations in Figs. 2(a)–2(c), the carrier density in Fig. 2(d) shows a monotonic steplike decrease starting from an initial value of $N \sim 5.2 \times 10^{17}$ cm^{-3}, besides the injection of additional carriers at $t = 40$ ps.

To visualize the carrier dynamics in the parabolic bands, Fig. 2(e) shows the energy-dependent carrier inversion as a function of time in a semilogarithmic contour plot. The inversion is defined as $n_{e\mathbf{k}} + n_{h\mathbf{k}} - 1$, where $n_{c\mathbf{k}}$ with $c \in \{e, h\}$ is the occupation probability of electrons and
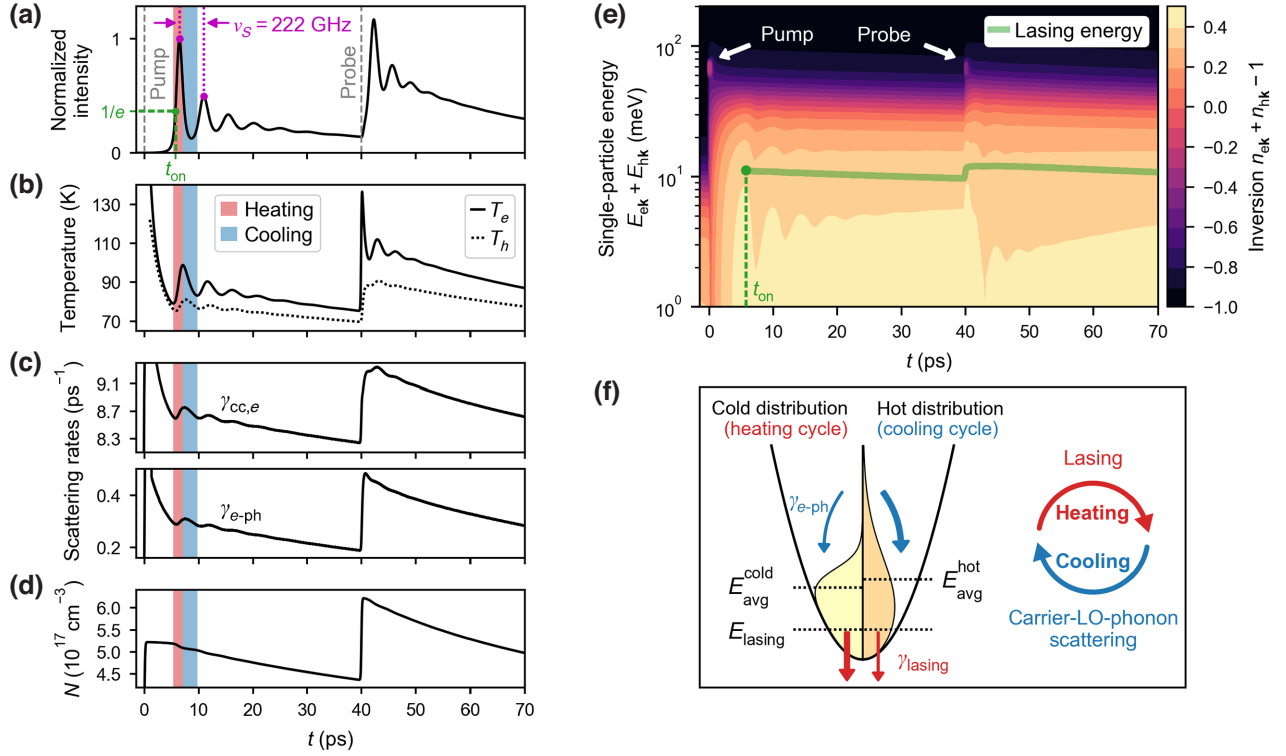
FIG. 2.   Quantum statistical simulation of the time-resolved pump-probe response. (a) The time-dependent output intensity for a pump-probe delay of $\Delta t = 40$ ps. From the first output pulse, we determine t_{on} and the oscillation frequency ν_S. (b)–(d) The corresponding time-dependent electron (T_e) and hole (T_h) temperature, carrier-carrier scattering rate of electrons ($\gamma_{cc,e}$), electron-LO-phonon scattering rate ($\gamma_{e\text{-ph}}$), and carrier density (N). In (a)–(d), the shaded areas highlight the first heating and cooling cycle of T_e. (e) Energy-resolved inversion, illustrating the time-dependent carrier dynamics. Here, $n_{c\mathbf{k}}$ and $E_{c\mathbf{k}}$, with $c \in \{e, h\}$, are, respectively, the occupation probability and energy of electrons and holes with wave vector $\mathbf{k}$. (f) A sketch of the oscillation mechanism, enabled by the exceptionally large modal-confinement factor Γ of NW lasers. Here, γ_{lasing} is the stimulated emission rate of the lasing mode with energy E_{lasing}, while E_{avg}^{cold} and E_{avg}^{hot} are the average kinetic energies of the respective distributions.

holes with wave vector $\mathbf{k}$. The corresponding electron and hole energies are denoted by $E_{c\mathbf{k}}$ with $c \in \{e, h\}$. The optical pump-probe excitation is indicated by white arrows. Within a few picoseconds, relaxation of the injected carriers (see Sec. VI of the Supplemental Material [32]) leads to a build-up of inversion at the lasing energy (solid green line). After the onset of lasing (t_{on}, green point), clear oscillations of the inversion are visible, which are directly connected to the carrier-temperature oscillations in Fig. 2(b). From Fig. 2(e), we further observe no signs of spectral hole burning. This results from the fast carrier-carrier scattering, which continuously thermalizes the electron-hole plasma, and the low end-facet reflectivity R, which reduces the stimulated emission rate (γ_{lasing}).

To explain the origin of these oscillations, Fig. 2(f) shows a schematic representation of two electron distributions having similar densities in the conduction band, one characterized by a lower T_e (yellow) than the other (orange). The lasing energy (E_{lasing}) is below the respective average kinetic energy (E_{avg}^{cold}, E_{avg}^{hot}). Thus, stimulated emission at a rate γ_{lasing} heats the remaining electron distribution [40–45]. In the event that this heating via

γ_{lasing} is sufficiently strong to overcome the cooling via $\gamma_{e\text{-ph}}$, T_e rises. Consequently, $\gamma_{e\text{-ph}}$ increases, whereas γ_{lasing} decreases due to the reduction in material gain (G_{mat}) [40,41]. Partial recovery of G_{mat} via $\gamma_{e\text{-ph}}$ then restarts the cycle. A similar discussion applies to holes.

However, in previous investigations of microcavity and nanoscale lasers, this intuitive effect of ultrafast self-induced temperature oscillations has been strongly damped, preventing the observation of sustained oscillations [24,44–47]. We explain the observations in Figs. 2(a)–2(e) for NW lasers by noting that the modal gain (G_{mod}) and G_{mat} are linked by $G_{mod} \propto \Gamma \cdot G_{mat}$, where Γ is the modal-confinement factor [48]. The corresponding differential gains with respect to the carrier temperature (T_c, with $c \in \{e, h\}$) are, therefore, to a good approximation related by $\partial G_{mod}/\partial T_c \propto \Gamma \cdot \partial G_{mat}/\partial T_c$. Thus, large Γ leads to enhanced interactions between the lasing mode and the gain material. For NW lasers, this effect is especially pronounced due to their wavelength-scale dimensions and unique resonator geometry, which allows exceptionally strong mode confinement with $\Gamma > 1$ [6,49,50]. We further note that the large Γ of NW lasers is, in

part, due to the strong lateral optical confinement and the resulting strongly nonparaxial mode propagation [49,50]. Moreover, here, there exists a balanced interplay between the rates of stimulated emission, carrier-carrier scattering, and carrier-LO-phonon scattering. As mentioned above, the carrier-carrier scattering is sufficiently fast to maintain Fermi-Dirac distributions and heating via stimulated emission is strong enough to compete with cooling via carrier-LO-phonon scattering, such that light-matter coupling is manifested as a strongly oscillating carrier temperature. In our NW lasers, it is precisely this combination of large Γ with these carrier dynamics that leads to the observed sustained oscillations. The important role of Γ has been confirmed by a comparison of the simulated laser dynamics with $\Gamma = 1.2$ (used here) and $\Gamma = 0.12$, which clearly demonstrates that the oscillations disappear for weaker mode confinement (see Sec. VII of the Supplemental Material [32]).

C. Excitation-power and lattice-temperature dependence

To test the above hypothesis for the origin of the observed ultrafast oscillations, we have experimentally studied the excitation-power and T_L dependence of the NW-laser dynamics and compared with the predictions of the quantum statistical model.

Figure 3 presents the results of the excitation-power-dependence measurement, with which we have investigated in detail how the lasing dynamics depend on N and γ_{lasing}. As shown in Fig. 3(a), t_{on} decreases from (9.9 ± 0.4) ps to (5.5 ± 0.4) ps as the pumping level increases from $P_{\text{pump}}/P_{\text{th}} \sim 1.8$ to 3.0. This decrease is in excellent quantitative agreement with theory. It results from the

increase in N with increasing $P_{\text{pump}}/P_{\text{th}}$, allowing the laser to turn on at higher carrier temperatures.

To estimate the frequency (f_E) of the oscillations in $|G^{(1)}(\Delta t, \tau)|$ from our measurements, we have determined the time interval between the main sideband and the first oscillation above (see Sec. VIII of the Supplemental Material [32]). As shown in Fig. 3(b), f_E increases with stronger excitation power from (231 ± 14) GHz to (344 ± 18) GHz. Since $|G^{(1)}(\Delta t, \tau)|$ and, thus, the simulated oscillation frequency (f_S) cannot be directly obtained from the quantum statistical model, we have computed the oscillation frequency ν_S. Here, we observe an increase from approximately 166 GHz to approximately 238 GHz, over the same range of excitation powers. Nonetheless, an approximate relationship between ν_S and f_S can be established using the semiconductor Bloch model. In the present case, f_S is related to ν_S by $f_S = 1.38 \cdot \nu_S$ (see Sec. IX of the Supplemental Material [32]). Applying this relationship to the frequencies ν_S in Fig. 3(b) leads to remarkable quantitative agreement between f_S and f_E over the entire range of excitation powers. The increase of the oscillation frequencies with stronger excitation power results from the complex interplay of various effects. As the main reason, we have identified the increased γ_{lasing}, leading to enhanced carrier-temperature oscillations and, hence, shorter heating and cooling cycles.

Complementary to the excitation-power series, varying T_L has allowed us to tune $\partial G_{\text{mat}}/\partial T_c$ and to shift the operating point of the laser toward higher carrier temperatures. All experimental data in Fig. 4 have been measured with $P_{\text{pump}}/P_{\text{th}} \sim 2.5$ and $P_{\text{probe}}/P_{\text{th}} \sim 0.5$. For illustration, Fig. 4(a) presents the measured $|G^{(1)}(\Delta t, \tau)|$ for $T_L = 40$ K, 60 K and 80 K. As T_L increases, the data show that t_{on} decreases, f_E increases and t_{pulse}
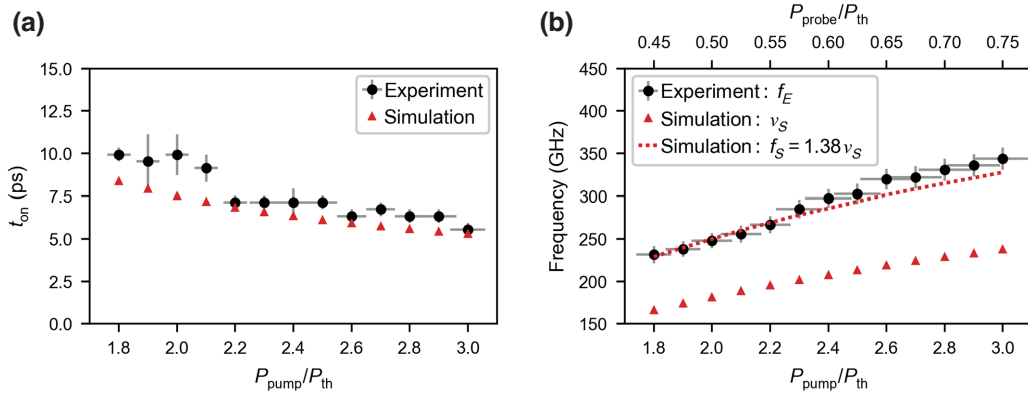

FIG. 3. The excitation-power dependence of the NW-laser dynamics. (a) A stronger pump pulse power ($P_{\text{pump}}/P_{\text{th}}$) produces a greater initial carrier density N, allowing the laser to turn on faster. Here, $P_{\text{probe}}/P_{\text{th}} \sim 0.5$ has been kept constant. (b) The increase in oscillation frequencies with excitation power depends on a complex interplay of several effects but is mainly driven by the increased stimulated emission rate γ_{lasing}. Here, we have kept the ratio $P_{\text{pump}}/P_{\text{probe}} = 4 : 1$ constant to ensure that the intensities of both output pulses remain comparable. All error bars represent 95% confidence intervals (CIs) of the mean and result from the methods used to determine P_{th}, t_{on} and f_E, as described in Secs. I, II, and VIII, respectively, of the Supplemental Material [32]. In (b), the uncertainty in excitation power refers to the bottom axis.
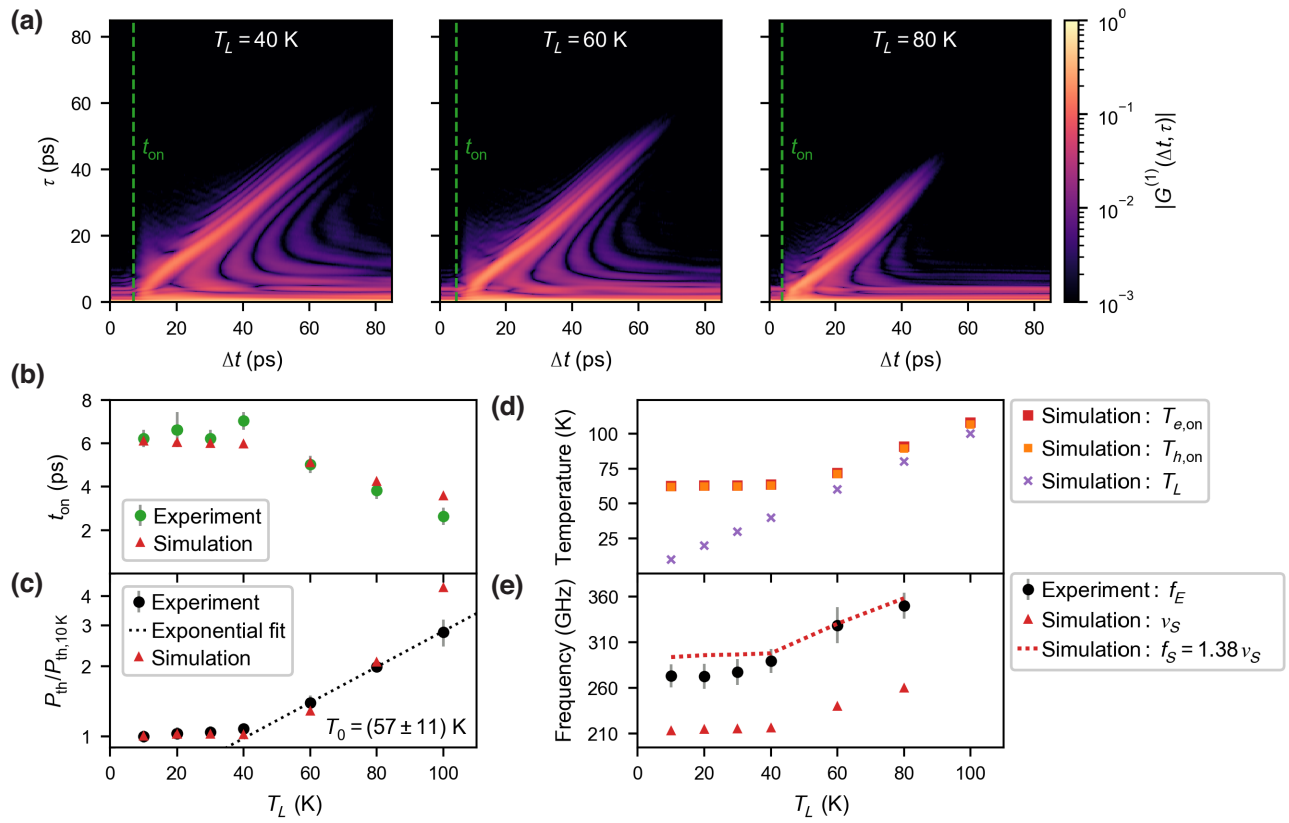
FIG. 4.   The lattice-temperature dependence of the NW-laser dynamics. (a) Three exemplary pump-probe measurements, illustrating the changes that occur with increasing T_L. (b) As T_L increases, t_{on} is at first constant and then decreases. (c) Above 40 K, P_{th} increases with a characteristic temperature T_0, as obtained from an exponential fit. This increase leads to the decrease of t_{on} in (b). The data have been normalized to the smallest threshold ($P_{th,10 K}$). (d) The electron ($T_{e,on}$) and hole ($T_{h,on}$) temperatures at times $t = t_{on}$ as a function of T_L, in which the excitation power has been set to $P_{pump}/P_{th} \sim 1$. The rise of $T_{e,on}$ and $T_{h,on}$ causes the increase of P_{th} in (c). (e) The oscillation frequencies increase as the lasing mode shifts toward the high-energy side of the gain spectrum, where $\partial G_{mat}/\partial T_c$ is larger. All error bars represent 95% CIs of the mean and result from the methods used to determine P_{th}, t_{on}, and f_E, as described in Secs. I, II, and VIII, respectively, of the Supplemental Material [32]. In (c), some error bars are smaller than the symbol size.

decreases (see Sec. X of the Supplemental Material [32]).

As shown by the data in Fig. 4(b), t_{on} remains approximately constant at approximately 6 ps up to 40 K and then decreases to (2.6 ± 0.4) ps as T_L increases further to 100 K. This behavior can be understood on the basis of the T_L dependence of P_{th}, shown in Fig. 4(c). For $T_L \leq$ 40 K, P_{th} remains almost constant, whereas at higher T_L it increases exponentially, with a characteristic temperature $T_0 = (57 \pm 11)$ K. Since the pumping level is fixed relative to P_{th}, this increase leads to a larger initial N. Consequently, t_{on} decreases, as observed in Fig. 4(b). The simulations presented in Figs. 4(b) and 4(c) quantitatively reproduce the experimental data and, thus, confirm our interpretation.

The T_L dependence of P_{th} is, in turn, accounted for by the variation of the electron ($T_{e,on}$) and hole ($T_{h,on}$) temperatures at laser turn-on, as shown in Fig. 4(d). For increasing T_L, they are initially constant at approximately 62 K, reflecting the fact that the cooling rate due to

carrier-LO-phonon scattering decreases rapidly for low carrier temperatures ($\lesssim 50$ K) [36,38]. Both $T_{e,on}$ and $T_{h,on}$ only rise as T_L becomes comparable, shifting the operating point of the laser toward higher carrier temperatures. The carrier distributions therefore spread out toward higher energies, which reduces G_{mat} at the lasing energy for a given N. Hence, P_{th} increases, explaining the observed trend in Fig. 4(c).

We are now in a position to explain the T_L dependence of the oscillation frequencies in Fig. 4(e). Up to 40 K, f_E remains approximately constant at approximately 270 GHz and then increases to (350 ± 20) GHz at $T_L = 80$ K. Similarly, ν_S increases from 213 GHz to 259 GHz. We have again calculated f_S from ν_S, using the proportionality factor of 1.38 stated above, and we have obtained remarkable agreement with f_E. The trend of the oscillation frequencies is strongly influenced by the T_L dependence of P_{th} in Fig. 4(c). As P_{th} increases, the correspondingly larger initial N blue shifts the lasing mode due to the associated change in refractive index and broadens the gain

spectrum as a result of band-gap renormalization and band filling. Simultaneously, the band gap and the lasing mode red shift with increasing T_L, the red shift of the lasing mode being smaller than the other effects. In combination, these processes effectively shift the lasing mode toward the high-energy side of the gain spectrum, where $\partial G_{\mathrm{mat}}/\partial T_c$ is larger. This leads to the observed increase in oscillation frequencies. No oscillations have been observed for $T_L = 100$ K, which coincides with the laser becoming multimodal. In addition, as shown in Fig. 4(d), the carrier temperatures increase for higher T_L, which reduces $\partial G_{\mathrm{mat}}/\partial T_c$ [51]. This counteracts the increases due to the shift of the lasing mode toward the high-energy side of the gain spectrum and at some point will compensate them. The oscillations are therefore expected to disappear at sufficiently high T_L, here > 80 K.

III. DISCUSSION AND CONCLUSIONS

In summary, we have investigated the microscopic lasing dynamics of GaAs-AlGaAs core-shell NW lasers. Thereby, we have demonstrated how a large Γ, and the consequently large $\partial G_{\mathrm{mod}}/\partial T_c$, can lead to exceptionally strong nonequilibrium laser dynamics. These manifest themselves as carrier-temperature oscillations through a dynamic competition between carrier heating via stimulated emission and carrier cooling via carrier-LO-phonon scattering. The results of our combined experimental and theoretical approach are consistent with oscillation frequencies ranging from 160 GHz to 260 GHz. Furthermore, our results indicate that coherent effects do not play a significant role in GaAs-AlGaAs core-shell NW lasers, thus challenging the interpretation proposed in previous work [23], which has been based on a significantly longer dephasing time.

Following the promising results of this work, one possible next step would be to directly time resolve the emission of a single GaAs-AlGaAs core-shell NW laser. Here, one of the challenges is to obtain a sufficient signal-to-noise ratio, since the volume and thus the output-emission intensity of NW lasers is relatively small [33]. Such a measurement would allow a direct experimental validation of the simulated data shown in Fig. 2(a).

Since the described dynamics involve oscillations of the carrier temperature and not the carrier density, they circumvent the speed limitations inherent in conventional relaxation oscillations [51]. For direct laser modulation based on changing the carrier density, the relaxation oscillation frequency determines the maximum modulation speed, which is currently limited to < 60 GHz without photonic feedback effects [52]. Similarly, we believe that the oscillation frequencies described here determine the ultimate speed limit for laser intensity or phase modulation based on changing the carrier temperature. We therefore anticipate that NW lasers could substantially

improve previously proposed laser-modulation schemes based on terahertz heating fields [51]. This is because their large $\partial G_{\mathrm{mod}}/\partial T_c$ makes them highly susceptible to applied electric fields. In such a scheme, an externally applied terahertz heating field modulates the carrier temperature and thus the laser output, avoiding the speed bottleneck of interband modulation [51]. This also creates further opportunities for ultrafast pulse shaping of nanoscale semiconductor lasers and, provided that the modulation depth is sufficient, would allow the generation of picosecond pulse trains with extremely high repetition rates > 100 GHz. In perspective, further research could achieve ultrafast modulation of NW lasers integrated into silicon photonic circuits [4].

The dynamics described above are substantially different from the expected class-B dynamics that are typical for semiconductor lasers and usually described by a standard rate-equation approach [48]. In our case, however, such an approach is insufficient. First, the predicted overall output-pulse length and shape well above threshold would not correspond well to our experimental observations [3,6]. Second, relaxation oscillations would be too slow to explain the observed dynamics [52]. Third, they would not be expected following excitation with femtosecond pulses [3,6]. This has made it necessary to go beyond such a rate-equation approach and the corresponding small-signal response theory to be able to describe our experimentally observed dynamics. It is, nevertheless, important to note that the rate-equation approach can be augmented to include temperature effects. This can either be done by, e.g., introducing a gain-saturation parameter [48] or by including the carrier temperature directly as a dynamical variable [53]. However, this requires the introduction of additional phenomenological parameters and would still need a self-consistent inclusion of many-body effects in order to yield predictions that can be quantitatively compared with experiments. Microscopic models, such as those used in the present work [31,54], solve these issues and allow a detailed description of nanoscale lasers on picosecond time scales while minimizing the number of free phenomenological parameters.

We note that our theoretical models [31,54] are general and thus allow our findings to be applied to other types of semiconductor lasers as well. There are several points to consider in the development of semiconductor lasers that are intended to be highly susceptible to externally applied terahertz fields. According to the key insight of this work, such a laser should have a large Γ. This can be achieved by an optimized spatial overlap of the lasing mode and the gain material, which simultaneously also decreases the threshold [49,50]. The choice of the gain material is crucial as well, as it directly affects the cooling rate of the carriers via carrier-LO-phonon scattering, which is mediated by the Fröhlich interaction. Moreover, the operating point of the carrier density and temperature should be chosen

such that $\partial G_{\mathrm{mod}}/\partial T_c$ is maximized. According to a previous theoretical investigation, this is the case when both the carrier density and temperature are as low as possible [51]. The differential modal gain can further be optimized by tuning the cavity length to place the lasing mode on the high-energy side of the gain spectrum [46,47,55]. Lastly, the laser must have a large enough resonator bandwidth and should preferentially be single mode. Both points can be achieved by making the laser as short as possible, which, of course, must be balanced with the simultaneously increasing threshold. Taken together, our work thus opens up further approaches to how the miniaturization of semiconductor lasers can be used to design their ultrafast dynamical properties.

This is complementary to previous research that has investigated accelerated laser dynamics based on Purcell enhancement [56,57] and plasmonic effects [17,58]. We note that no Purcell enhancement is expected for our NW lasers, since their effective mode volume is approximately 140 times larger than that of the photonic crystal laser studied in Ref. [56]. Other approaches to ultrafast laser modulation, which typically require larger device structures, include the use of photonic feedback effects [52] and mode field switching [59]. It is noteworthy that with both photonic feedback on a silicon carbide substrate [52] and Purcell enhancement in a GaAs material system [56], modulation frequencies of up to approximately 100 GHz have been demonstrated, although the latter could not be confirmed theoretically [60,61].

Practical applications, of course, would ultimately require ultrafast modulation of nanolasers at room temperature. The current drawback of the dynamics described in our work is the limitation to $T_L \leq 80$ K. However, this could be overcome by using a low-dimensional gain medium, such as multiple quantum wells [13], simultaneously allowing emission-wavelength tuning toward the technologically relevant telecom bands [15,16].

IV. MATERIALS AND METHODS

A. Growth

The investigated NW lasers have been grown in a two-step axial and radial growth process on silicon using molecular-beam epitaxy [3,5]. These NWs have a length in the range of 10–16 μm and a diameter of approximately 340 nm [5].

B. Optical characterization

For the optical investigations, the NWs have been transferred onto a sapphire substrate, providing excellent heat conductivity at cryogenic temperatures and sufficient refractive index contrast to achieve lasing. The samples have been mounted inside a liquid helium flow cryostat and all experiments reported in this work have been performed within a temperature range of 10–100 K. Single NWs have been excited using 200 fs optical pulses (repetition frequency of 82 MHz), delivered by a mode-locked laser, which were focused to a spot diameter of 17 μm, covering the entire NW. The detection spot was centered on one of the end facets of the NW and had a diameter of 11 μm. We have determined the threshold (P_{th}) of the NWs using single-pulse excitation (see Sec. I of the Supplemental Material [32]). To study their ultrafast dynamics, we have performed nonresonant degenerate pump-probe spectroscopy and measured the spectrally resolved and time-integrated NW-laser emission. The spectra have been recorded as a function of pump-probe delay Δt using a double spectrometer and a CCD camera. The delay has been adjusted using an optical delay line with a bidirectional precision < 10 fs. With a spectral resolution of $\Delta E < 40$ μeV, interference fringes resulting from pulse separations > 100 ps could be resolved.

C. Numerical modeling

With our modeling approach, we have reproduced the characteristic features of the experiments and, thereby, made deductions about the underlying carrier and carrier-field interaction dynamics. In a complete semiclassical description, the light-matter interaction is governed by the semiconductor Maxwell-Bloch equations, in which the carrier-carrier and carrier-phonon interactions are described by the proper collision integrals in the Boltzmann-equation framework. However, the direct simulation of the experiment at hand turns out to be too computationally expensive when using this complete approach. We have therefore conducted two different model simplifications, depending on the physical feature that was to be investigated. To study the dynamics of the emitted electric field, we have used a relaxation-rate approximation for the scattering dynamics, using precalculated values (see Sec. IV of the Supplemental Material [32]), while keeping the full semiconductor Maxwell-Bloch equation [31]. We refer to this as the semiconductor Bloch model (see Sec. XI of the Supplemental Material [32]). In contrast, to study the carrier dynamics in detail, we have eliminated the polarization dynamics and resorted to the field intensity for the light-matter interaction. While this approach cannot describe the dynamics of the electric field or potential coherent transients, it has allowed us to keep the full Boltzmann-equation framework for the carrier dynamics with reasonable computational effort [24,30,31,43,54,62–64]. We refer to this as the quantum statistical model (see Sec. XII of the Supplemental Material [32]). Both models use the same set of simulation parameters, tabulated in Sec. III of the Supplemental Material [32]. In addition, we note that both models use the same simplified description of the band structure. Due to the proximity of our excitation to the band edge (electron excess energy approximately 60 meV,

heavy-hole excess energy approximately 11 meV), we have been able to neglect the split-off band and use the parabolic band approximation [65]. Valence-band warping has been neglected as well, as it has been shown to have no substantial effect on carrier distributions for times longer than approximately 200 fs after photoexcitation [66]. Moreover, the light-hole band has also been neglected due to the ratio of the carrier density in the light-hole band compared to the carrier density in the heavy-hole band being only approximately 12% [31]. The dynamics are thus dominated by the heavy-hole band. The validity of this approximation is retrospectively established through the good agreement of our theoretical models with the experimental results.

ACKNOWLEDGMENTS

[1] R. Chen, T.-T. D. Tran, K. W. Ng, W. S. Ko, L. C. Chuang, F. G. Sedgwick, and C. Chang-Hasnain, Nanolasers grown on silicon, Nat. Photon. **5,** 170 (2011).

[2] H. Sun, F. Ren, K. W. Ng, T.-T. D. Tran, K. Li, and C. J. Chang-Hasnain, Nanopillar lasers directly grown on silicon with heterostructure surface passivation, ACS Nano **8,** 6833 (2014).

[3] B. Mayer, L. Janker, B. Loitsch, J. Treu, T. Kostenbader, S. Lichtmannecker, T. Reichert, S. Morkötter, M. Kaniber, G. Abstreiter, C. Gies, G. Koblmüller, and J. J. Finley, Monolithically integrated high-β nanowire lasers on silicon, Nano Lett. **16,** 152 (2016).

[4] T. Stettner, T. Kostenbader, D. Ruhstorfer, J. Bissinger, H. Riedl, M. Kaniber, G. Koblmüller, and J. J. Finley, Direct coupling of coherent emission from site-selectively grown III-V nanowire lasers into proximal silicon waveguides, ACS Photon. **4,** 2537 (2017).

[5] B. Mayer, D. Rudolph, J. Schnell, S. Morkötter, J. Winnerl, J. Treu, K. Müller, G. Bracher, G. Abstreiter, G. Koblmüller, and J. J. Finley, Lasing from individual GaAs-AlGaAs core-shell nanowires up to room temperature, Nat. Commun. **4,** 2931 (2013).

[6] D. Saxena, S. Mokkapati, P. Parkinson, N. Jiang, Q. Gao, H. H. Tan, and C. Jagadish, Optically pumped room-temperature GaAs nanowire lasers, Nat. Photon. **7,** 963 (2013).

[7] M. A. Zimmler, J. Bao, F. Capasso, S. Müller, and C. Ronning, Laser action in nanowires: Observation of the transition from amplified spontaneous emission to laser oscillation, Appl. Phys. Lett. **93,** 051101 (2008).

[8] J. C. Johnson, H.-J. Choi, K. P. Knutsen, R. D. Schaller, P. Yang, and R. J. Saykally, Single gallium nitride nanowire lasers, Nat. Mater. **1,** 106 (2002).

[9] M. H. Huang, S. Mao, H. Feick, H. Yan, Y. Wu, H. Kind, E. Weber, R. Russo, and P. Yang, Room-temperature ultraviolet nanowire nanolasers, Science **292,** 1897 (2001).

[10] X. Duan, Y. Huang, R. Agarwal, and C. M. Lieber, Single-nanowire electrically driven lasers, Nature **421,** 241 (2003).

[11] A. H. Chin, S. Vaddiraju, A. V. Maslov, C. Z. Ning, M. K. Sunkara, and M. Meyyappan, Near-infrared semiconductor subwavelength-wire lasers, Appl. Phys. Lett. **88,** 163115 (2006).

[12] S. Geburt, A. Thielmann, R. Röder, C. Borschel, A. McDonnell, M. Kozlik, J. Kühnel, K. A. Sunter, F. Capasso, and C. Ronning, Low threshold room-temperature lasing of CdS nanowires, Nanotechnology **23,** 365204 (2012).

[13] T. Stettner, P. Zimmermann, B. Loitsch, M. Döblinger, A. Regler, B. Mayer, J. Winnerl, S. Matich, H. Riedl, M. Kaniber, G. Abstreiter, G. Koblmüller, and J. J. Finley, Coaxial GaAs-AlGaAs core-multishell nanowire lasers with epitaxial gain control, Appl. Phys. Lett. **108,** 011108 (2016).

[14] D. Saxena, N. Jiang, X. Yuan, S. Mokkapati, Y. Guo, H. H. Tan, and C. Jagadish, Design and room-temperature operation of GaAs/AlGaAs multiple quantum well nanowire lasers, Nano Lett. **16,** 5080 (2016).

[15] T. Stettner, A. Thurn, M. Döblinger, M. O. Hill, J. Bissinger, P. Schmiedeke, S. Matich, T. Kostenbader, D. Ruhstorfer, H. Riedl, M. Kaniber, L. J. Lauhon, J. J. Finley, and G. Koblmüller, Tuning lasing emission toward long wavelengths in GaAs-(In,Al)GaAs core-multishell nanowires, Nano Lett. **18,** 6292 (2018).

[16] P. Schmiedeke, A. Thurn, S. Matich, M. Döblinger, J. J. Finley, and G. Koblmüller, Low-threshold strain-compensated InGaAs/(In,Al)GaAs multi-quantum well nanowire lasers emitting near 1.3 μm at room temperature, Appl. Phys. Lett. **118,** 221103 (2021).

[17] T. P. H. Sidiropoulos, R. Röder, S. Geburt, O. Hess, S. A. Maier, C. Ronning, and R. F. Oulton, Ultrafast plasmonic nanowire lasers near the surface plasmon frequency, Nat. Phys. **10,** 870 (2014).

[18] R. Röder, T. P. H. Sidiropoulos, C. Tessarek, S. Christiansen, R. F. Oulton, and C. Ronning, Ultrafast dynamics of lasing semiconductor nanowires, Nano Lett. **15,** 4637 (2015).

[19] M. Wille, C. Sturm, T. Michalsky, R. Röder, C. Ronning, R. Schmidt-Grund, and M. Grundmann, Carrier density driven

lasing dynamics in ZnO nanowires, Nanotechnology **27,** 225702 (2016).

[20] J. C. Blake, J. Nieto-Pescador, Z. Li, and L. Gundlach, Ultraviolet femtosecond Kerr-gated wide-field fluorescence microscopy, Opt. Lett. **41,** 2462 (2016).

[21] R. Hollinger, Z. Samsonova, D. Gupta, C. Spielmann, R. Röder, L. Trefflich, C. Ronning, and D. Kartashov, Enhanced absorption and cavity effects of three-photon pumped ZnO nanowires, Appl. Phys. Lett. **111,** 213106 (2017).

[22] J. C. Blake, J. Nieto-Pescador, Z. Li, and L. Gundlach, Femtosecond luminescence imaging for single nanoparticle characterization, J. Phys. Chem. A **124,** 4583 (2020).

[23] B. Mayer, A. Regler, S. Sterzl, T. Stettner, G. Koblmüller, M. Kaniber, B. Lingnau, K. Lüdge, and J. J. Finley, Long-term mutual phase locking of picosecond pulse pairs generated by a semiconductor nanowire laser, Nat. Commun. **8,** 15521 (2017).

[24] H. C. Schneider, F. Jahnke, and S. W. Koch, Microscopic theory of non-equilibrium microcavity laser dynamics, Quantum Semiclass. Opt. **9,** 693 (1997).

[25] J. L. Oudar, D. Hulin, A. Migus, A. Antonetti, and F. Alexandre, Subpicosecond Spectral Hole Burning Due to Nonthermalized Photoexcited Carriers in GaAs, Phys. Rev. Lett. **55,** 2074 (1985).

[26] J. L. Oudar, A. Migus, D. Hulin, G. Grillon, J. Etchepare, and A. Antonetti, Femtosecond Orientational Relaxation of Photoexcited Carriers in GaAs, Phys. Rev. Lett. **53,** 384 (1984).

[27] R. Binder, D. Scott, A. E. Paul, M. Lindberg, K. Henneberger, and S. W. Koch, Carrier-carrier scattering and optical dephasing in highly excited semiconductors, Phys. Rev. B **45,** 1107 (1992).

[28] T. Elsaesser, J. Shah, L. Rota, and P. Lugli, Initial Thermalization of Photoexcited Carriers in GaAs Studied by Femtosecond Luminescence Spectroscopy, Phys. Rev. Lett. **66,** 1757 (1991).

[29] J. Shah, *Ultrafast Spectroscopy of Semiconductors and Semiconductor Nanostructures*, Springer Series in Solid-State Sciences Vol. 115 (Springer-Verlag, Berlin, 1999).

[30] F. Jahnke and S. W. Koch, Many-body theory for semiconductor microcavity lasers, Phys. Rev. A **52,** 1712 (1995).

[31] W. W. Chow, S. W. Koch, and M. Sargent, *Semiconductor-Laser Physics* (Springer-Verlag, Berlin, 1994).

[32] See the Supplemental Material at http://link.aps.org/supplemental/10.1103/PhysRevApplied.20.034045 for details, including: single-pulse excitation and the laser threshold (Sec. I); the experimental determination of the turn-on time (Sec. II); continuous-wave lasing characteristics (Sec. III); semiconductor Bloch simulation of the time-resolved pump-probe response (Sec. IV); determination of the carrier temperature (Sec. V); carrier relaxation (Sec. VI); the influence of the confinement factor on the lasing dynamics (Sec. VII); the determination of the oscillation frequency (Sec. VIII); comparison of the electric field and intensity autocorrelation (Sec. IX); the output pulse length as a function of the lattice temperature (Sec. X); the semiconductor Bloch model with relaxation-rate approximation (Sec. XI); and the quantum statistical model (Sec. XII). The Supplemental Material includes Refs. [67–90].

[33] R. Röder and C. Ronning, Review on the dynamics of semiconductor nanowire lasers, Semicond. Sci. Technol. **33,** 033001 (2018).

[34] R. Loudon, *The Quantum Theory of Light* (Oxford University Press, Oxford, 2000).

[35] D. Saxena, F. Wang, Q. Gao, S. Mokkapati, H. H. Tan, and C. Jagadish, Mode profiling of semiconductor nanowire lasers, Nano Lett. **15,** 5342 (2015).

[36] R. Leheny, J. Shah, R. Fork, C. Shank, and A. Migus, Dynamics of hot carrier cooling in photo-excited GaAs, Solid State Commun. **31,** 809 (1979).

[37] K. Leo and W. Rühle, Influence of carrier lifetime on the cooling of a hot electron-hole plasma in GaAs, Solid State Commun. **62,** 659 (1987).

[38] J. Shah and R. C. C. Leite, Radiative Recombination from Photoexcited Hot Carriers in GaAs, Phys. Rev. Lett. **22,** 1304 (1969).

[39] J. Shah, Hot electrons and phonons under high intensity photoexcitation of semiconductors, Solid-State Electron. **21,** 43 (1978).

[40] M. P. Kesler and E. P. Ippen, Subpicosecond gain dynamics in GaAlAs laser diodes, Appl. Phys. Lett. **51,** 1765 (1987).

[41] M. S. Stix, M. P. Kesler, and E. P. Ippen, Observations of subpicosecond dynamics in GaAlAs laser diodes, Appl. Phys. Lett. **48,** 1722 (1986).

[42] B. Gomatam and A. DeFonzo, Theory of hot carrier effects on nonlinear gain in GaAs-GaAlAs lasers and amplifiers, IEEE J. Quantum Electron. **26,** 1689 (1990).

[43] F. Jahnke and S. W. Koch, Theory of carrier heating through injection pumping and lasing in semiconductor microcavity lasers, Opt. Lett. **18,** 1438 (1993).

[44] G. Pompe, T. Rappen, and M. Wegener, Transient response of an optically pumped short-cavity semiconductor laser, Phys. Rev. B **51,** 7005 (1995).

[45] F. Jahnke, H. C. Schneider, and S. W. Koch, Combined influence of design and carrier scattering on the ultrafast emission dynamics of quantum well microcavity lasers, Appl. Phys. Lett. **69,** 1185 (1996).

[46] P. Michler, A. Lohner, W. W. Rühle, and G. Reiner, Transient pulse response of $In_{0.2}Ga_{0.8}As$/GaAs microcavity lasers, Appl. Phys. Lett. **66,** 1599 (1995).

[47] P. Michler, M. Hilpert, W. W. Rühle, H. D. Wolf, D. Bernklau, and H. Riechert, Emission dynamics of $In_{0.2}Ga_{0.8}As$/GaAs λ and 2λ microcavity lasers, Appl. Phys. Lett. **68,** 156 (1996).

[48] L. A. Coldren, S. W. Corzine, and M. L. Mašanović, *Diode Lasers and Photonic Integrated Circuits* (Wiley, Hoboken, New Jersey, 2012).

[49] A. Maslov and C. Ning, Modal gain in a semiconductor nanowire laser with anisotropic bandstructure, IEEE J. Quantum Electron. **40,** 1389 (2004).

[50] C. Z. Ning, Semiconductor nanolasers, Phys. Status Solidi B **247,** 774 (2010).

[51] J. Li and C. Z. Ning, Plasma heating and ultrafast semiconductor laser modulation through a terahertz heating field, J. Appl. Phys. **88,** 4933 (2000).

[52] S. Yamaoka, N.-P. Diamantopoulos, H. Nishi, R. Nakao, T. Fujii, K. Takeda, T. Hiraki, T. Tsurugaya, S. Kanazawa, H. Tanobe, T. Kakitsuka, T. Tsuchizawa, F. Koyama, and S. Matsuo, Directly modulated membrane lasers with 108

GHz bandwidth on a high-thermal-conductivity silicon carbide substrate, Nat. Photon. **15,** 28 (2021).

[53] C. Z. Ning, R. A. Indik, and J. V. Moloney, Self-consistent approach to thermal effects in vertical-cavity surface-emitting lasers, J. Opt. Soc. Am. B **12,** 1993 (1995).

[54] F. Jahnke, K. Henneberger, W. Schäfer, and S. W. Koch, Transient nonequilibrium and many-body effects in semiconductor microcavity lasers, J. Opt. Soc. Am. B **10,** 2394 (1993).

[55] A. Grabmaier, G. Fuchs, A. Hangleiter, R. W. Glew, P. D. Greene, and J. E. A. Whiteaway, Linewidth enhancement factor and carrier-induced differential index in InGaAs separate confinement multi-quantum-well lasers, J. Appl. Phys. **70,** 2467 (1991).

[56] H. Altug, D. Englund, and J. Vučković, Ultrafast photonic crystal nanocavity laser, Nat. Phys. **2,** 484 (2006).

[57] B. Romeira and A. Fiore, Purcell effect in the stimulated and spontaneous emission rates of nanoscale semiconductor lasers, IEEE J. Quantum Electron. **54,** 1 (2018).

[58] J. B. Khurgin and G. Sun, Comparative analysis of spasers, vertical-cavity surface-emitting lasers and surface-plasmon-emitting diodes, Nat. Photon. **8,** 468 (2014).

[59] D. Pellegrino, P. Busi, F. Pagliano, B. Romeira, F. W. van Otten, A. Y. Silov, and A. Fiore, Mode-field switching of nanolasers, APL Photon. **5,** 066109 (2020).

[60] T. Suhr, N. Gregersen, K. Yvind, and J. Mørk, Modulation response of nanoLEDs and nanolasers exploiting Purcell enhanced spontaneous emission, Opt. Express **18,** 11230 (2010).

[61] N. Gregersen, T. Suhr, M. Lorke, and J. Mørk, Quantum-dot nano-cavity lasers with Purcell-enhanced stimulated emission, Appl. Phys. Lett. **100,** 131107 (2012).

[62] K. Henneberger, F. Herzel, S. W. Koch, R. Binder, A. E. Paul, and D. Scott, Spectral hole burning and gain saturation in short-cavity semiconductor lasers, Phys. Rev. A **45,** 1853 (1992).

[63] K. Henneberger, F. Jahnke, and F. Herzel, Many-body effects and multi-mode behaviour in semiconductor lasers, Phys. Status Solidi B **173,** 423 (1992).

[64] F. Jahnke, S. W. Koch, and K. Henneberger, Dynamic response of short-cavity semiconductor lasers, Appl. Phys. Lett. **62,** 2313 (1993).

[65] J. S. Blakemore, Semiconducting and other major properties of gallium arsenide, J. Appl. Phys. **53,** R123 (1982).

[66] M. A. Osman, M. Cahay, and H. L. Grubin, Effect of valence band anisotropy on the ultrafast relaxation of photoexcited electrons in GaAs, Solid-State Electron. **32,** 1911 (1989).

[67] P. T. Landsberg, Electron interaction effects on recombination spectra, Phys. Status Solidi B **15,** 623 (1966).

[68] R. Martin and H. Stormer, On the low energy tail of the electron-hole drop recombination spectrum, Solid State Commun. **22,** 523 (1977).

[69] H. Kalt and M. Rinker, Band-gap renormalization in semiconductors with multiple inequivalent valleys, Phys. Rev. B **45,** 1139 (1992).

[70] R. Röder, M. Wille, S. Geburt, J. Rensberg, M. Zhang, J. G. Lu, F. Capasso, R. Buschlinger, U. Peschel, and C.

[71] R. Pässler and G. Oelgart, Appropriate analytical description of the temperature dependence of exciton peak positions in GaAs/Al$_x$Ga$_{1-x}$As multiple quantum wells and the $\Gamma_{8v} - \Gamma_{6c}$ gap of GaAs, J. Appl. Phys. **82,** 2611 (1997).

[72] F. K. Reinhart, A heuristic approach to precisely represent optical absorption and refractive index data for photon energies below, at, and above the band gap of semiconductors: The case of high-purity GaAs. Part I, J. Appl. Phys. **97,** 123534 (2005).

[73] F. K. Reinhart, A heuristic approach to determine the modifications of electronic and optical properties of "intrinsic" GaAs under free-carrier injection. Part II, J. Appl. Phys. **97,** 123535 (2005).

[74] I. Vurgaftman, J. R. Meyer, and L. R. Ram-Mohan, Band parameters for III-V compound semiconductors and their alloys, J. Appl. Phys. **89,** 5815 (2001).

[75] G. A. Samara, Temperature and pressure dependences of the dielectric constants of semiconductors, Phys. Rev. B **27,** 3494 (1983).

[76] D. Strauch and B. Dorner, Phonon dispersion in GaAs, J. Phys. Condens. Matter **2,** 1457 (1990).

[77] F. Jahnke and S. W. Koch, Ultrafast intensity switching and nonthermal carrier effects in semiconductor microcavity lasers, Appl. Phys. Lett. **67,** 2278 (1995).

[78] T. Elsaesser, J. Shah, L. Rota, and P. Lugli, Initial Thermalization of Photoexcited Carriers in GaAs Studied by Femtosecond Luminescence Spectroscopy, Phys. Rev. Lett. **66,** 1757 (1991).

[79] M. G. Kane, K. W. Sun, and S. A. Lyon, Ultrafast carrier-carrier scattering among photoexcited nonequilibrium carriers in GaAs, Phys. Rev. B **50,** 7428 (1994).

[80] V. Korenman, Nonequilibrium quantum statistics; Application to the laser, Ann. Phys. **39,** 72 (1966).

[81] W. Schäfer and J. Treusch, An approach to the nonequilibrium theory of highly excited semiconductors, Z. Phys. B Condens. Matter **63,** 407 (1986).

[82] K. Henneberger and H. Haug, Nonlinear optics and transport in laser-excited semiconductors, Phys. Rev. B **38,** 9759 (1988).

[83] F. Herzel, K. Henneberger, and W. Vogel, The semiconductor laser linewidth: A Green's function approach, IEEE J. Quantum Electron. **29,** 2891 (1993).

[84] U. Mohideen, R. E. Slusher, F. Jahnke, and S. W. Koch, Semiconductor Microlaser Linewidths, Phys. Rev. Lett. **73,** 1785 (1994).

[85] T. Visser, H. Blok, B. Demeulenaere, and D. Lenstra, Confinement factors and gain in optical amplifiers, IEEE J. Quantum Electron. **33,** 1763 (1997).

[86] H. Haug and S. W. Koch, *Quantum Theory of the Optical and Electronic Properties of Semiconductors* (World Scientific, Singapore, 2009), 5th ed.

[87] J. Collet and T. Amand, Model calculation of the laser-semiconductor interaction in subpicosecond regime, J. Phys. Chem. Solids **47,** 153 (1986).

[88] J. Collet, T. Amand, and M. Pugnet, Numerical approach to non-equilibrium carrier relaxation in picosecond

and subpicosecond physics, Phys. Lett. A **96**, 368 (1983).

[89] C. L. Collins and P. Y. Yu, Generation of nonequilibrium optical phonons in GaAs and their application in study-

ing intervalley electron-phonon scattering, Phys. Rev. B **30**, 4501 (1984).

[90] E. Rosencher and B. Vinter, *Optoelectronics* (Cambridge University Press, Cambridge, United Kingdom, 2002).